Effect of Al^{3+} Co-doping on the Dopant Local Structure, Optical Properties, and Exciton Dynamics in Cu^{+}-Doped ZnSe Nanocrystals

Sheraz Gul,[†,‡] Jason Kyle Cooper,[†] Per-Anders Glans,[§] Jinghua Guo,[§] Vittal K. Yachandra,[‡] Junko Yano,[‡,*] and Jin Zhong Zhang[†,*]

[†]Department of Chemistry and Biochemistry, University of California, Santa Cruz, California 95064, United States, [§]Advanced Light Source, Lawrence Berkeley National Laboratory, Berkeley, California 94720, United States, and [‡]Physical Biosciences Division, Lawrence Berkeley National Laboratory, Berkeley, California 94720, United States

ABSTRACT The dopant local structure and optical properties of Cu-doped ZnSe (ZnSe:Cu) and Cu and Al co-doped ZnSe (ZnSe:Cu,Al) nanocrystals (NCs) were studied with an emphasis on understanding the impact of introducing Al as a co-dopant. Quantum-confined NCs with zinc blende crystal structure and particle size of 6 ± 0.6 Å were synthesized using a wet chemical route. The local structure of the Cu dopant, studied by extended X-ray absorption fine structure, indicated that Cu in ZnSe:Cu NCs occupies a site that is neither substitutional nor interstitial and is adjacent to a Se vacancy. Additionally, we estimated that approximately 25 ± 8% of Cu was located on the surface of the NC. Al^{3+} co-doping aids in Cu doping by accounting for the charge imbalance originated by Cu^{+} doping and consequently reduces surface Cu doping. The Cu ions remain distorted from the center of the tetrahedron to one of the triangular faces. The lifetime of the dopant-related photoluminescence was found to increase from 550 ± 60 to 700 ± 60 ns after Al co-doping. DFT calculations were used to obtain the density of states of a model system to help explain the optical properties and dynamics processes observed. This study demonstrates that co-doping using different cations with complementary oxidation states is an effective method to enhance optical properties of doped semiconductor NCs of interest for various photonics applications.

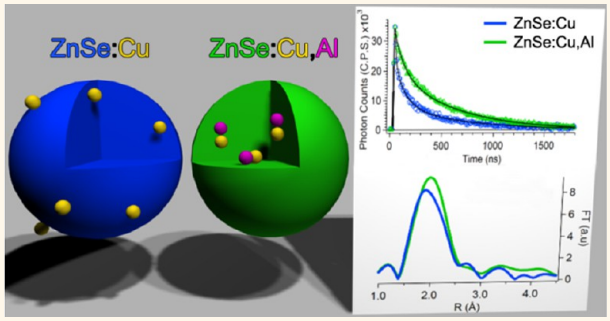

KEYWORDS: doped semiconductor nanocrystals · copper doped · ZnSe · co-doped · EXAFS · exciton dynamics

Colloidal semiconductor nanocrystals (NCs) or quantum dots (QDs) have been studied extensively due to their potential applications in economical, solution-processable devices. The intriguing optical and electronic properties of the NCs, originating from quantum confinement effects and large surface-to-volume ratio,[1−7] make them emerging candidates for applications in solid-state lightening,[8,9] biomedical labeling,[10−12] photovoltaics,[13,14] lasers,[1] and electronics.[15] Their properties can be varied in a controllable manner by changing the size, shape, or surface functionalization and/or by introducing small quantities of dopant atoms. Doped semiconductor NCs constitute an important subclass of nanomaterials where a small amount of impurities are intentionally incorporated into the host material, thus adding another degree of freedom for altering their optical, electronic, and magnetic properties.[16−20] Doped nanomaterials possess unique properties that are important for imminent applications, including longer excited state lifetimes, minimum self-absorption, broad emission spectral window, and thermal stability.[21−24]

Copper-doped II−VI semiconductor NCs have been the subject of great interest in recent years due to their potential as bright visible light phosphors with size-tunable emission.[22,25,26] The low toxicity and large Stokes shift of the Cu related emission in Cu-doped ZnSe NCs make them an attractive candidate for lighting and display applications.[27,28] However, the synthesis of

* Address correspondence to jyano@lbl.gov; zhang@ucsc.edu.

Received for review June 10, 2013 and accepted September 12, 2013.

Published online September 12, 2013
10.1021/nn402932q

Cu-doped ZnSe can be quite challenging because there is a large difference in the solubilities of copper selenide and zinc selenide (with K_{sp} values of $10^{-57.7}$ and 3.6×10^{-26}, respectively),[29,30] which renders their co-precipitation rather difficult. As observed in our recent study, copper enters ZnSe as Cu^{+} and mostly stays on or closer to the surface of the host.[31] The +1 oxidation state would require the copper ion to accompany defect structures, specifically selenium vacancies (V_{Se}), for charge compensation. A possible route to stabilize Cu in the host lattice could be co-doping with a group III element, which accounts for the charge imbalance and acts as a coactivator as well. Coactivators have been found to introduce donor levels just below the conduction band (CB)[32] and enhance the donor−acceptor pair (DAP) emission, which is the primary emission seen in these systems.[33]

To better implement the approaches for the rational design of these doped semiconductor NCs, it is critical to improve the understanding of the optical properties of this class of NCs, which depend strongly upon the local structure around the luminescence centers. The local structure around the dopant ions is influenced by the oxidation state mismatch and the ionic size difference between the dopant and the host cation. Photogenerated electrons and holes are expected to decay through these impurity ion luminescence centers with different transition probability and decay rates as compared to the host. Especially for NCs, the optical properties and dynamical processes will be sensitive to the local structure of the dopant atoms due to a strong interaction between the quantum-confined exciton and the dopant site. Therefore, it is extremely important to obtain a clear, atomic level picture of the local structure surrounding the Cu ion in these systems, including the location of dopant ion in the NCs, local distortions in bond distances, and oxidation state of the dopant. Since the concentration of Cu is relatively low in these materials (0.5% of the total Zn content) and because it is difficult to differentiate between Zn and Cu by standard X-ray diffraction (XRD), extended X-ray absorption fine structure (EXAFS) as an element-specific technique that is sensitive only to the first few neighboring shells emerges as one of the most powerful techniques to resolve the local structure around the Cu atoms. Although some studies have been done on Cu-doped ZnS NCs,[34,35] such detailed investigation of the Cu-doped ZnSe system is lacking.

In conjunction with the structural properties' studies, the investigation of optical properties of the ZnSe:Cu and ZnSe:Cu,Al systems using steady-state and time-resolved photoluminescence techniques can help to gain insight into the correlation between the structural and optical properties as well as the associated electronic energy levels. In addition, dynamics studies of the exciton or charge carriers can provide useful information about the various photophysical processes involved. For example, it has been reported previously that the inclusion of Cu in ZnSe can extend the fluorescence lifetime from 10 ns to 600 ns.[31] This effect was attributed to the transient formation of Cu^{2+} after the hole becomes trapped by Cu^{+}, forming a stable hole state within the NCs. These studies are aimed at optimizing the photoluminescence properties for potential functional applications of the doped semiconductor NCs.

In the present work, we have synthesized and determined the local structure of the dopant ion in ZnSe:Cu and ZnSe:Cu,Al NCs using EXAFS. X-ray absorption near edge structure (XANES) have been used to determine the oxidation states of the dopant and co-dopant in these NCs. Their optical properties have also been characterized with emphasis on photoluminescence. In addition, the exciton and charge carrier dynamics of these NCs have been investigated using time-correlated single-photon counting (TCSPC) combined with integrated singular value decomposition (SVD) global fitting to elucidate the wavelength dependence of the fluorescence recombination pathways, thereby allowing for a regimented correlation between their structural and optical/dynamic properties. Furthermore, density functional theory (DFT) calculations aimed at understanding the electronic structure of the Cu related states have been performed using structural information obtained by EXAFS to gain a precise picture about the active energy levels involved during electronic transitions. EXAFS studies indicated that Cu impurity occupies a site that is neither an interstitial site nor a high-symmetry substitutional. Most importantly, co-doping with Al eliminated anion vacancies around the Cu site and improved the photoluminescence (PL) yield by increasing the lifetime of Cu-related emission.

RESULTS AND DISCUSSION

UV−Visible Absorption and PL. The UV−visible absorption spectra of both the ZnSe:Cu and ZnSe:Cu,Al samples are shown in Figure 1(a). The spectra show an absorption onset around 422 nm and a first exciton peak around 403 nm, which is due to the band edge excitation of the host and exhibits quantum confinement effects. The first exciton peak position indicates that both the samples have comparable particle size. There are no noticeable differences between the absorption spectra of the two samples, indicating that Al co-doping has essentially no effect on the electronic absorption spectrum of ZnSe, which is not unusual.

The PL spectra shown in Figure 1(b) exhibit a broad emission peak (fwhm ~80 nm) centered at 540 and 530 nm for the ZnSe:Cu and ZnSe:Cu,Al, respectively. The samples show minimal host-related emission at 430 nm, indicating complete Cu doping in both cases. There is no considerable difference in the spectral features between the two samples with similar optical density (0.2 OD) at the excitation wavelength of

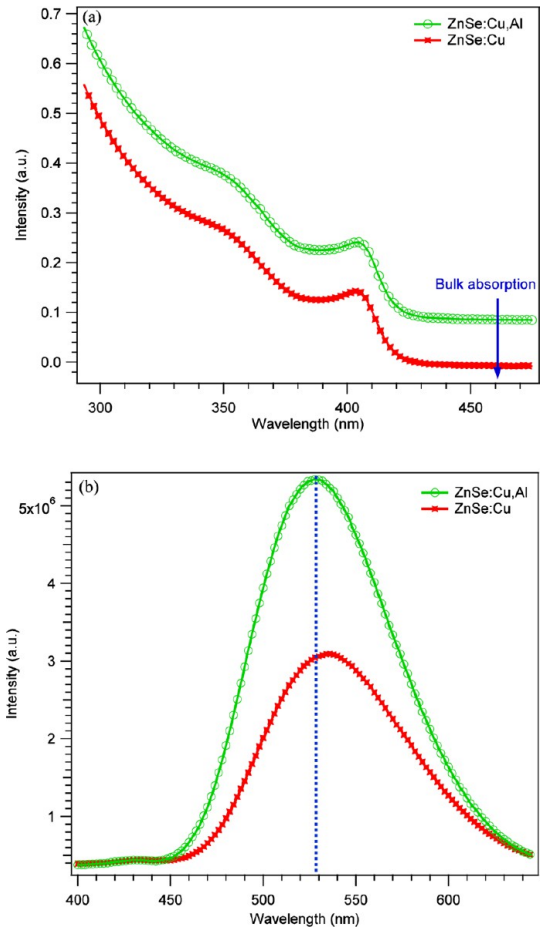

Figure 1. (a) UV−visible absorption spectra of ZnSe:Cu (red) and ZnSe:Cu,Al (green) samples indicating that there is no considerable change in the absorption after co-doping. (b) PL spectra of the two samples with the same optical density at an excitation energy of 390 nm. The PL gets blue-shifted, and the quantum yield is almost doubled with Al co-doping.

390 nm. It is evident that the samples differ in PL quantum yield (QY): about 3% for ZnSe:Cu NCs and 7% after co-doping with Al. The lower QY in ZnSe:Cu is likely due to electron trap states associated with V_{Se} defects that originate from the charge compensation required as a result of the Cu^{+}-doping. Introducing Al^{3+} would account for the charge imbalance, resulting in the removal of these trap states thereby decreasing the trap-mediated nonradiative electron−hole recombination. The PL emission in Cu-doped ZnSe has been attributed to the electronic transition from the CB or a shallow donor level, optionally introduced by the co-dopant or unintentionally by oxygen,[36] to the Cu d-states.[37] The PL arises from the initial photoexcitation of a valence band (VB) electron to the CB in the host ZnSe. The CB electron then might get trapped by shallow trap (ST) states, surface dangling bond (DB) states, or impurity donors such as Al or oxygen. The hole generated in the VB then moves to Cu^{+}, creating a transient Cu^{2+} acceptor state. Depending upon the ligand geometry surrounding the Cu, the d-states of Cu^{2+} are split by the ligand field, resulting in multiple possible hole acceptor states, which has been previously regarded as the reason for the broad Cu-related emission band, with a fwhm of ~80 nm. The PL was seen to slightly blue-shift after Al co-doping, as indicated by the vertical line in Figure 1(b). This suggests that the donor states originating from Al are more shallow than the donor states involved in the ZnSe:Cu sample.

Crystal Structure, Size, and Composition. Powder XRD patterns for both samples are shown in Figure 2(a), which correspond to zinc blende ZnSe structure, according to the data in the Joint Committee on Powder Diffraction Standards Card (File No. 80-0021). Peaks corresponding to the (111), (220), and (311) lattice planes are indexed. No change in the crystalline phase is observed by co-doping with Al. Using the Debye−Scherrer formula, the crystallite size of the NCs was calculated to be ~6 nm from the line width of the (111) peak. A representative TEM image of the ZnSe:Cu,Al NCs is presented in Figure 2(b) along with the histogram and a HRTEM image as the insets. The diameters of 100 particles were measured using the ImageJ program[38] (distributed by NIH) to obtain the histogram. The average particle size was determined to be 6 nm with a size distribution of ~10%, as shown in the inset of Figure 2(b). It is clear from the HRTEM image and from XRD that Cu did not precipitate as a separate phase, *i.e.*, copper selenide as a separate particle or on the surface of the ZnSe NCs. The TEM data regarding the ZnSe:Cu sample are reported in Figure 2(c), it is clear that the particle size and the size distribution profile are almost the same as those of ZnSe:Cu,Al. In fact, the size and size distribution is quite reporoducible with our synthesis procedure regardless of the small amounts of added impurities as seen in our previous study,[31] which focuses on ZnSe:Cu NCs.

The relative concentrations of Zn, Se, Cu, and Al were measured using inductively coupled plasma optical emission spectrometry (ICP-OES), the results of which are presented in Table 1. The Zn:Se ratio and relative Cu percent were essentially the same between the ZnSe:Cu and ZnSe:Cu,Al samples. Additionally, the results confirm the presence of Al in the co-doped system at a similar mole ratio to the Cu, indicating that Cu and Al dope into ZnSe as 1:1. This result confirms our previous assertion that Cu dopes ZnSe as a monovalent cation, requiring charge balance by the trivalent Al cation.

Cu and Al K-Edge XANES. The Cu K-edge XANES spectra of the two samples are presented in Figure 3(a) along with the standard samples including Cu foil and Cu_2Se. XANES is sensitive to the nature of chemical bonding, oxidation state, and local structure around the atom being probed. The fine structure of the spectrum for ZnSe:Cu,Al differs considerably from that of the ZnSe:Cu in the energy range 8986−8997 eV, indicating that Al is incorporated in the vicinity of the Cu ion. The fine

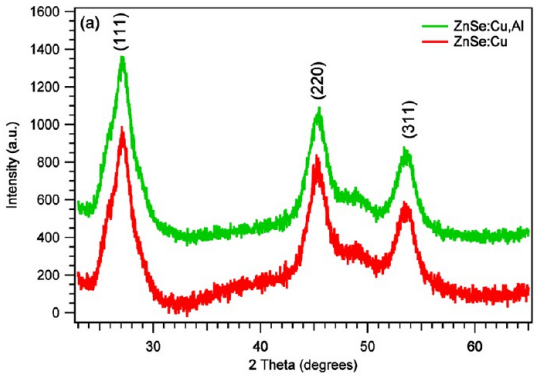

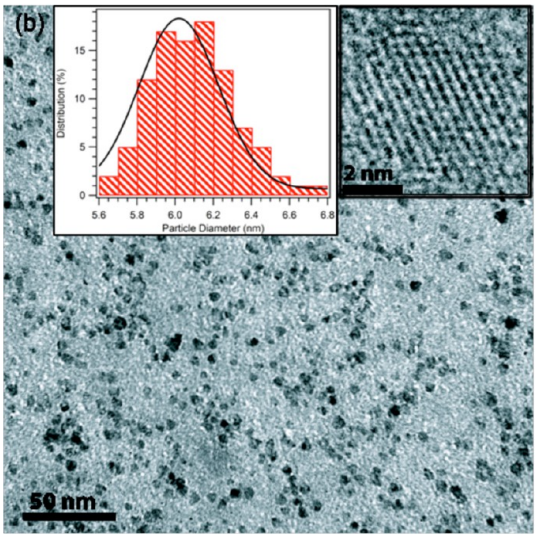

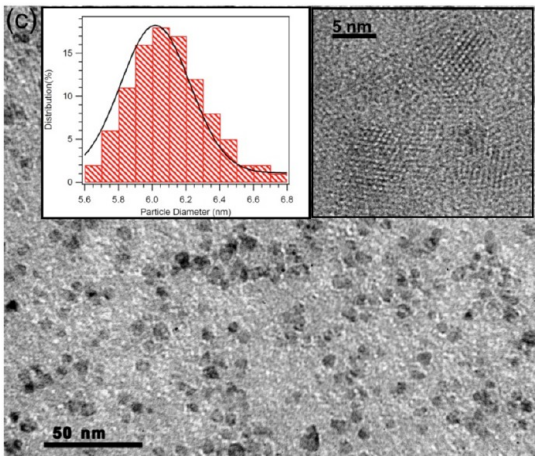

Figure 2. (a) XRD pattern of ZnSe:Cu (red) and ZnSe:Cu,Al (green) samples exhibiting zinc blende crystal structure. (b) TEM image of ZnSe:Cu,Al NCs with the inset showing the HRTEM image of a single nanocrystal along with the histogram. (c) Representative TEM image of ZnSe:Cu NCs with the insets showing histogram and an HRTEM image.

structure of Cu_2Se is quite different from both of the Cu-doped NC samples. However, the edge position is consistent with the +1 oxidation state of Cu.[39] Also, in the case of K-edges of transition metals with partially filled d-states, a pre-edge peak is observed due to transition from 1s → 3d states. Such transitions are

TABLE 1. ICP-OES Analysis of ZnSe:Cu and ZnSe:Cu,Al NCs

sample	molar Zn/Se ratio	% of Cu of total Zn content	% of Al of total Zn content
ZnSe:Cu	1.09	0.49	
ZnSe:Cu,Al	1.13	0.52	0.60

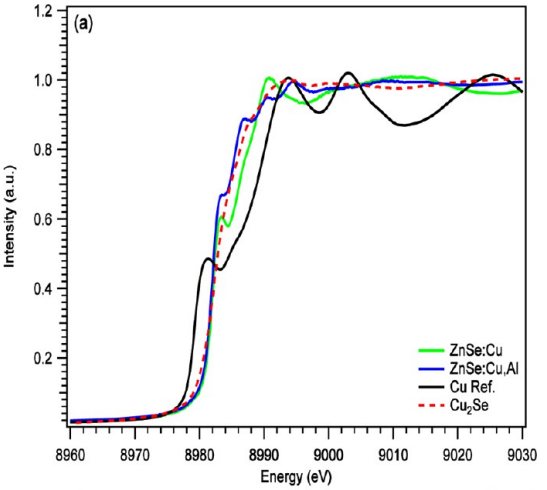

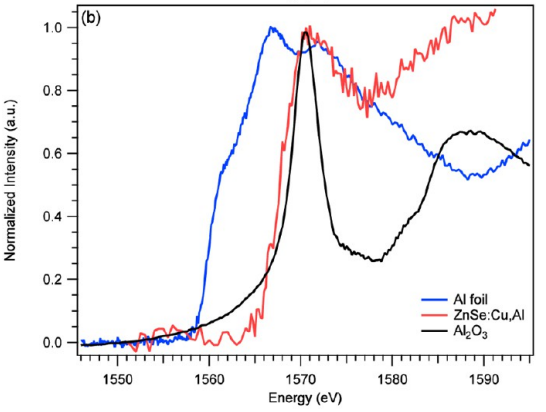

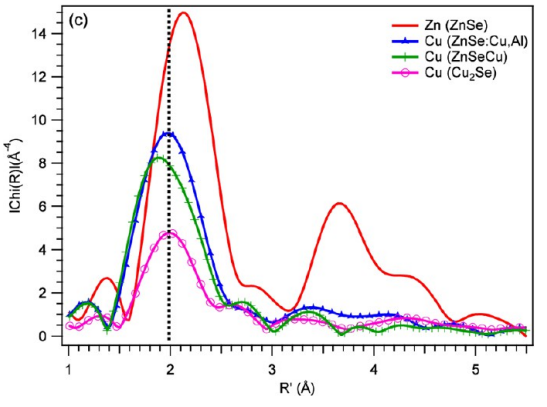

Figure 3. (a) Comparison of Cu K-edge XANES for ZnSe:Cu, ZnSe:Cu,Al, Cu_2Se, and Cu metal. The plots were normalized at higher energies. (b) XANES spectra at the Al K-edge for ZnSe:Cu,Al, Al_2O_3, and Al foil. The spectra indicate that Al exists in the +3 oxidation state in the NC sample and there is no clustering of elemental Al. (c) Magnitude of the Fourier transform of experimental EXAFS functions ($k^3\chi$) in ZnSe:Cu, ZnSe:Cu,Al, and Cu_2Se for the Cu K-edge along with that of the Zn K-edge of ZnSe NCs.

dipole forbidden, but become weakly allowed due to hybridization with p-states. In the case of the Cu K-edge, a pre-edge would be expected if the ion were in a +2 oxidation state ($3d^9$ electronic configuration), as reported in the case of Cu ions with empty d-states.[40,41] The absence of such a pre-edge peak in our data (Figure 3a) is further evidence of Cu being in the +1 oxidation state in these NCs.

To further confirm the Al co-doping, XANES spectra were measured at the Al K-edge and are presented in Figure 3(b) for the ZnSe:Cu,Al sample along with those of Al_2O_3 and Al foil. The absorption edge shifts to higher energies with increasing oxidation state. For the ZnSe:Cu,Al sample, the absorption edge appears at higher energy than elemental Al, which indicates that there is no clustering of Al. Also, the absorption edge for the NC sample starts around the same energy as that of Al_2O_3, which indicates that Al is in the +3 oxidation state in this sample. Although the signal-to-noise ratio is not very good in the case of the ZnSe:Cu,Al sample due to the low concetration of Al, it is quite obvious that the first peak is broad in the case of the NC sample and the fine structure differs from that of Al_2O_3, which further indicates that Al gets incorporated into the NCs and has a different local environment than Al in Al_2O_3.

EXAFS

The Fourier transforms (FT) of the Cu K-edge EXAFS data for the ZnSe:Cu and ZnSe:Cu,Al samples are shown in Figure 3(c) along with the Zn EXAFS from the ZnSe NCs as well as the Cu EXAFS from the Cu_2Se standard, for comparison. The EXAFS data at the Zn K-edge of the ZnSe:Cu NCs confirm that the Cu local structure in ZnSe:Cu is different from that of Zn and that the Cu doping is not a simple substitution of Zn. In Figure 3(c), the *x*-axis is the apparent distance, which is approximately 0.5 Å shorter than the actual distance due to the phase shift.[42] The first peak in these traces corresponds to the nearest neighbor Se atoms in cubic ZnSe. It is clear that the first peak positions for Cu are slightly shorter than that for Zn. Since Cu and Zn are neighboring elements in the periodic table and the backscattering atom is Se in all the cases here, the profound differences among the traces are due to different local structures around the absorbing atoms. In addition, the Cu EXAFS for the ZnSe:Cu and ZnSe:Cu,Al samples differ from each other; the peak in the former is asymmetric, appears at slightly shorter distance, and has lower amplitude as compared to the more symmetric peak of ZnSe:Cu,Al. The asymmetry and comparatively reduced amplitude in ZnSe:Cu indicate that there is more than one type of Cu center. Although the amplitudes are quite different, the first shell peak position for Cu_2Se aligns well with that of ZnSe:Cu,Al. This implies that Cu^+ ions in these two might occupy sites of similar symmetry.

Zn EXAFS. FEFF8 was used to construct the theoretical EXAFS paths from the ZnSe zinc blende structure, which was used as the starting model.[43] For fitting the Zn K-edge data of ZnSe NCs, three single scattering (SS) paths were used, which include Zn−Se (2.45 Å), Zn−Zn (4.00 Å), and a longer Zn−Se (4.70 Å), with the bond lengths being constrained to the cubic ZnSe structure (only allowing small variations). The amplitude reduction factor (S_0^2), which accounts for the many-body effects such as the shake up/off process at the absorbing atom, was obtained from the bulk ZnSe and fixed to 0.81. The coordination number (*N*) of the first shell was fixed to $N = 4$, while the *N* number of the second and third shell was allowed to vary since a considerable number of NC atoms are on the surface, which may lead to a reduced average number of second- and third-shell neighbors from $N = 12$ in the bulk. The fit obtained is shown in Figure 4(a), which agrees well with the experimental data. The values for the Debye−Waller factor (σ^2) were 0.004, 0.006, and 0.008 $Å^2$ for the three SS paths used. The complete results of the fit are reported in Table S1 of the Supporting Information and agree well with the experimentally determined parameters of bulk ZnSe, except that the number of second and third neighbors was found to be 9.1 ± 0.4 and 7.6 ± 0.4, respectively, which is less than that of bulk ZnSe ($N = 12$).[44,45]

Cu EXAFS. Since Cu^+ replaces a Zn^{2+} cation in the ZnSe lattice, a number of charge-compensated models have been proposed to correct the charge imbalance caused by Cu doping. The two primary models are (i) two Cu^+ ions replace two Zn^{2+} ions and an accompanying neighboring Se^{2-} vacancy ($V_{Se^{2-}}$) is created,[46] and (ii) one Cu^+ substitutes for one Zn^{2+} ion (Cu^+_{Zn}) and a second dopes at an interstitial site, Cu_i^+.[47,48]

Initially, theoretical EXAFS functions were calculated using FEFF8 starting from the known cubic ZnSe structure and replacing the central Zn atom with Cu. The S_0^2 parameter was determined empirically by fitting the Cu EXAFS data for CuSe (data not shown here) and was fixed to 0.83. Using these Cu−Se parameters from the ZnSe:Cu^+_{Zn} model, no reasonable fit could be obtained, as expected. One such fit is shown in Supplemental Figure S1 and Table S1 (ZnSe:Cu fit #1), in which the Cu−Se bond distances were allowed to vary during the fit procedure, as we expect Cu−Se to be shorter than Zn−Se. As mentioned, the FT first peak is asymmetric, indicating the contribution from more than one type of Cu center, likely from Cu atoms on the surface of the NC. In addition, the ΔE_0 value for this fit turns out to be quite large (−13.68 ± 4.0), which is another indication that Cu exists in more than one phase in this system. Consequently, we added a Cu−O path, which represents the surface Cu coordinated to octadecylamine, water, or oxygen (in the case where Cu gets oxidized). Also, the first neighbor peak (Cu−Se) is expected to be at a similar or

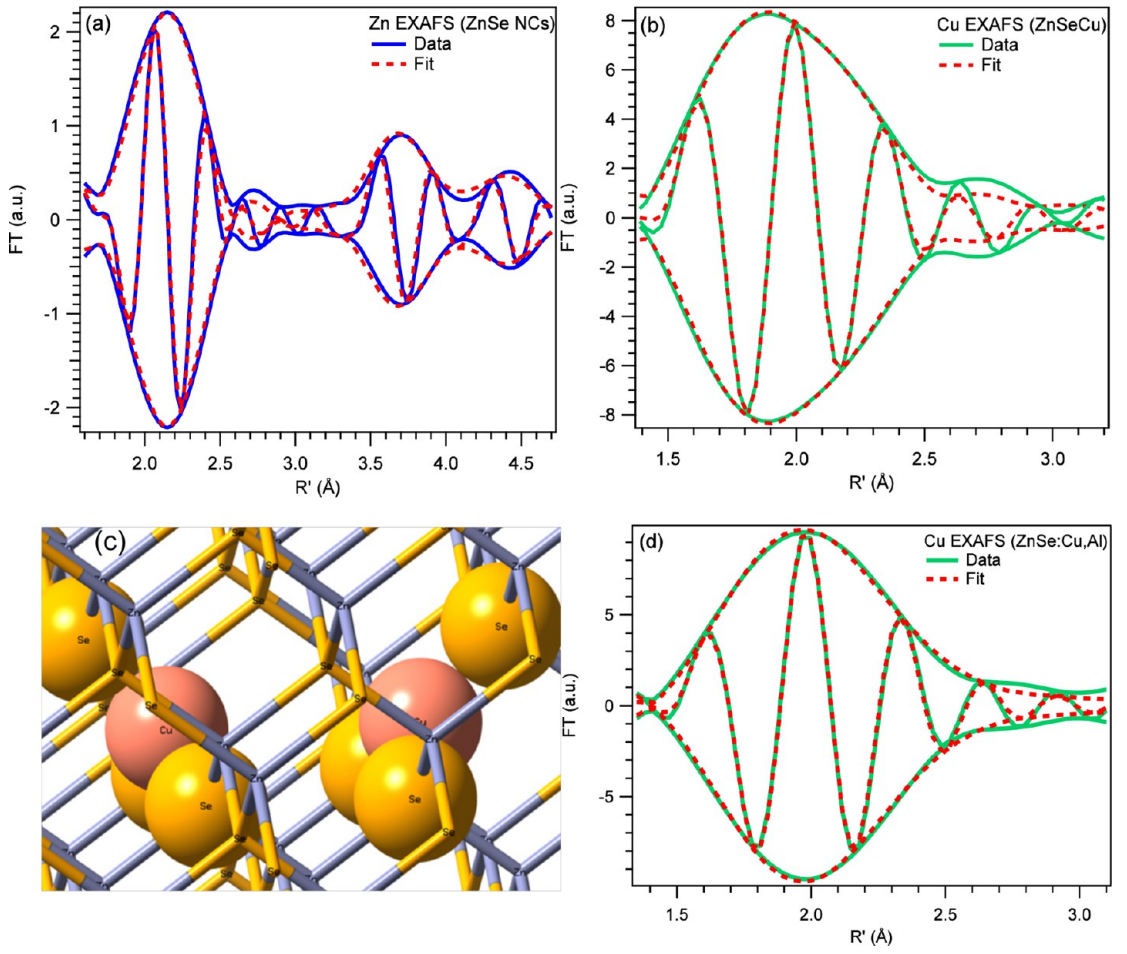

Figure 4. (a) *R*-space data (blue) for ZnSe NCs at the Zn K-edge along with the fit (red) carried over the *r*-space of 1.1−4.7 Å. The fast oscillation represents the real part of FT. The data were fit to a sum of three peaks: Zn−Se, Zn−Zn, and a longer Zn−Se (for the fit parameters see Supplemental Table S1, ZnSe NCs). (b) Fit #2 (red) of the Cu EXAFS data (green) for the ZnSe:Cu sample carried over the range 1.3−2.7 Å (see Supplemental Table S1, ZnSe:Cu fit #2). A Cu−O shell had to be included to account for the surface Cu content, which turned out to be 25 ± 8% of the total Cu. (c) Structural model for local structure around the core Cu showing two neighboring Cu ions accompanying a Se vacancy. Atom colors are Zn (purple), Se (yellow), and Cu (pink). (d) *R*-space data (green) for the ZnSe:Cu,Al sample including fit #2 (red) to the first shell, carried out over the range 1.3−2.7 Å. For this fit Cu−Se distances for three Se first neighbors were restrained around 2.34 Å, whereas the distance was allowed to vary for the fourth Se.

shorter bond distance compared to ZnSe; therefore, a variable parameter of Cu−Se bond distance was used during the fit. A good fit was obtained as shown in Figure 4(b) (Supplemental Table S1, ZnSe:Cu fit #2). For this fit, the reduced chi-square value decreased by more than half of its value by including a Cu−O path (χ^2_{red} decreased from 289 to 47), which indicates the validity of the additional path. With this fit, the number of nearest Cu−Se neighbors was found to be 2.7 ± 0.3 for the core Cu, while a shorter Cu−O fraction was about 0.9 ± 0.3. This implys that a major fraction of interior Cu must be accompanying a Se vacancy, and the surface Cu site was estimated to be 25 ± 8% of the total Cu content. A local structural model of internally doped Cu^{+}_{Zn} is shown in Figure 4(c) with two neighboring Cu ions along with the V_{Se}. The Cu−Se distance was found to be 2.34 Å, which is 0.11 Å shorter than the bond distance if Cu were substitutional to Zn (Zn−Se is ∼2.45 Å). A similar defect structure has been reported recently for Cu-doped ZnS which shows that Cu accompanies a Se vacancy.[49]

It is interesting to note that there is no second-neighbor peak in the ZnSe:Cu EXAFS. Even though a considerable amount of Cu is estimated to be on the surface, it is expected to have enough Cu−Zn second neighbors that would result in a second-neighbor peak.[49] However, if Cu is displaced away from a V_{Se} and gets closer to the remaining three Se by 0.11 Å, which corresponds to an off-center displacement of Cu by ∼0.46 Å, the 12 Zn second neighbors would no longer be equidistant from the absorbing Cu. In this case, the Zn second neighbors would contain three groups: three of them being around ∼3.6 Å from Cu, six with almost unchanged distance at ∼4.0 Å, and the remaining three at a distance of ∼4.4 Å. With such variability in the second-neighbor distances, the second neighbor peak would split by approximately 1/3 Å and the real parts of the FT would be out of phase for

each component, resulting in a small amplitude between 3 and 4 Å, as was seen in the *r*-space data. Using the parameters of this defect structure around Cu, a fit was carried out over the longer range of 1.1−4.4 Å and is shown in Figure S2 (Supplemental Table S1, ZnSe:Cu fit #3). The fit agrees well with the data having a small amplitude between 3 and 4 Å.

In the case of Cu_i^+, there are two possible interstitial sites in the zinc blende structure, as addressed by Goldman *et al.*[45] One of the interstitial sites has four Se nearest neighbors at 2.45 Å and six Zn neighbors at 2.83 Å, whereas the second site has four Zn nearest neighbors at 2.45 Å and six Se neighbors at 2.83 Å. FEFF8 was used to calculate the EXAFS functions for both Cu_i^+ possibilities by starting with the cubic ZnSe and placing the central Cu at an interstitial site. We carried out the fits by adding the Cu−Zn peak around 2.83 Å for Cu_i^+ and restraining the Cu−Zn pair distance to ±0.05 Å around the nominal distance. In all such fits, with varying fractions of Cu_i^+, the amplitude corresponding to the interstitial peak turns out to be negligible. Similar results were obtained for the second interstitial site with Zn first neighbors and Se second neighbors. Therefore, we concluded that the fraction of Cu_i^+, if present, is negligible.

For the ZnSe:Cu,Al sample, theoretical FEFF functions were generated from a model by starting with the cubic ZnSe structure, replacing one Zn with Cu and another Zn, in the nearest neighbor shell, by Al. No reasonable fit was obtained using these theoretical functions. The closest fit obtained for the first shell, when the Cu−Se distances were allowed to vary, is presented in Figure S3 of the Supporting Information. The coordination number of Cu−Se corresponding to this fit was 3.6 ± 0.3, and the *R*-factor value, which is a measure of the absolute misfit between the data and the fit, was 0.091 (Table S1, ZnSe:Cu,Al fit #1).

Another possibility could be considered based on the recent crystal structure studies of Cu_2Se by Gulay *et al.*[50] They reported that Se ions are in a close-packed arrangement, making layers in ABC sequence, with Cu ions occupying all the tetrahedral interstices. It was reported that, out of 12 Cu ions of the unit cell, 11 of them are shifted from the center of the tetrahedral site toward the edge or one of the faces of the tetrahedron. Not only are the individual Cu−Se bond distances different in this crystal structure, but also they are different from other Cu centers of the unit cell. Such anisotropic distribution of Cu could well explain the reduced amplitude of the first peak and the absence of the second neighbor peak in the FT of Cu_2Se EXAFS (Figure 3c), which further supports the argument above for the negligible amplitude of the second-neighbor peak in the NC sample. In addition, the amplitude of the peak for Cu in Cu_2Se is smaller than that in the NCs (Figure 3b). This might suggest that the Cu ions in the NCs have less anisotropy in their distribution and prefer a certain triangular plane of the tetrahedron, instead of a random distribution, as in Cu_2Se. This would further support the argument that Al occupies a site in the vicinity of Cu, causing it to prefer a particular triangular facet of the tetrahedron.

Keeping in view the crystal structure of Cu_2Se, we carried out another fit with two Cu−Se paths such that for the first path the Cu−Se distance was restrained around 2.34 Å, whereas the distance was allowed to vary for the second one.The resulting fit (fit #2) for the first shell is shown in Figure 4(d) and agrees very well with the data. For this fit, the Cu−Se distances are 2.35 Å, corresponding to a coordination number of 2.8 ± 0.2, and a second Cu−Se distance of ∼2.67 Å, corresponding to a coordination number of 0.9 ± 0.2 (Table S1, ZnSe:Cu,Al fit #2). This indicates that the Cu site is not exactly substitutional; not only does the Cu move closer to three Se, but the fourth Se likely becomes displaced from its position and moves toward the Cu as well. Again the displacement of Cu from the center of the tetrahedral site would split the Cu−Zn second-neighbor peak into three: one at a distance shorter than normal, one at almost the nominal pair distance, and the third one at a longer distance. Such a splitting is expected to reduce the amplitude for the second-neighbor peak as described earlier. This may be the reason that no substantial amplitude is observed between 3 and 4 Å in the *r*-space data, as exhibited in Figure 3(c). A fit carried over the longer range (1.1−4.4 Å) starting with the parameters corresponding to this distorted Cu site is shown in Figure S4 (Table S1, ZnSe:Cu,Al fit #3).

To find out the fraction of surface Cu in the ZnSe:Cu, Al sample, a Cu−O path was added in the EXAFS fitting. However, the quality of fit did not improve considerably; the contribution was negligible and an increase in reduced chi-square was observed. Therefore, we conclude that there is little surface Cu in this sample, if any. Hence, Al^{3+} not only compensates the charge imbalance but also enhances the solubility of the Cu in the host, resulting in internally doped NCs. As observed in the ZnSe:Cu, the inclusion of Cu_i^+ into the fitting model did not improve the fit.

DFT Calculation of Density of States. The electronic structure of the ZnSe NCs before and after Cu doping was studied using DFT with the PBE functional, ultrasoft pseudopotentials, and plane wave basis sets. The density of states (DOS) for the host material was calculated for a 64-atom supercell and is presented in Figure 5(a). The Cu-doped ZnSe NC system was studied with a 63-atom supercell in which two Zn atoms were replaced by Cu and the Cu−Se nearest neighbor distance was distorted to the bond distance measured by EXAFS, placing Cu in a distorted trigonal

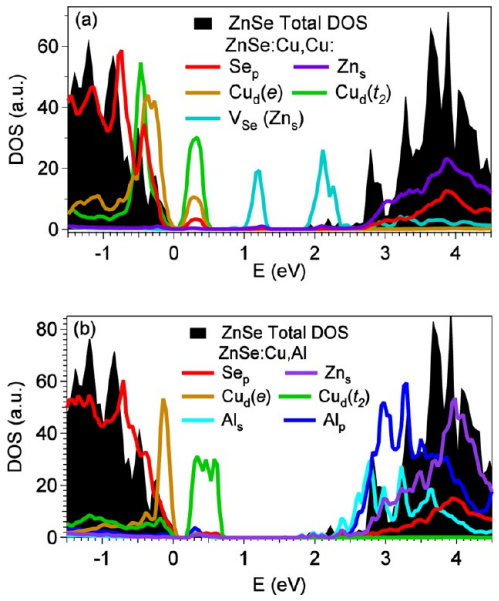

Figure 5. (a) Partial DOS for Se p (red) and Zn s (purple) and Cu e (brown) and t_2 (green) states, calculated with the 63-atom supercell, as well as for the V_{Se} state caused by Cu doping, which are related to the Zn s dangling bond orbital (blue). (b) Partial DOS for Se p (red), Zn s (purple), Cu e (brown), Cu t_2 (green), Al s (light blue), and Al p (dark blue) states.The total density of states (DOS) of ZnSe 64-atom supercell (solid black) shown in both (a/b).

geometry. The fourth Se, shared by both Cu dopants, was removed, forming a $V_{Se^{2-}}$. The Zn s and Se p DOS obtained from this calculation are shown in Figure 5(a). The VB is due to Se p-states while the CB is from strongly hybridized Se p and Zn s orbitals, as was also the case in the ZnSe system. The integrated local density of states (LDOS) can be seen in Figure 6. The Cu d(e) and d(t_2) DOS as well as the $V_{Se^{2-}}$ related states (which is the dangling bond Zn s orbital) are also shown. These states were multiplied by a scaling factor in order for them to be visible against the VB and CB states, making the vertical axis arbitrary in Figure 5.

The Cu $d_{x^2-y^2}$ and d_{z^2} orbitals (collectively, d(e)) were found to be strongly hybridized with the VB Se p-states and contribute to the VB edge. This result is contrary to the currently accepted model, which places the e orbitals above the VB edge.[26] The Cu d_{xz}, d_{yz}, and d_{xy} (t_2) states are found to be above the VB edge within the band gap (E_g). The five Cu d orbital DOS can be found in the Supplemental Figure S5. Using a Gaussian peak to fit the Cu t_2 DOS peaks, the Cu t_2 states are E_{VB} +0.31 eV and have a fwhm of 120 meV. The state associated with the V_{Se} has two energies, a bonding (V_{Se}) and an antibonding (V_{Se}*) configuration. This can be easily seen in the integrated LDOS plots shown in Figure 6. Using Gaussian peaks, the bonding orbital is E_{VB} +1.26 eV, while the antibonding state is E_{VB} +2.19 eV. For the sake of consistency in measuring the energy spacing between levels, Gaussian peaks were applied with the same fwhm as the Cu-related t_2 peak to fit the VB and CB edges. This allows us to measure peak-to-peak distances, which we take to be more consistent than the min, max, or average of a given state or band. The calculated E_g is 2.48 eV, while the quantum-confined experimental E_g is 3.07 eV. Taking the ratio between calculated and experimental E_g as a correction factor, we can assert that the Cu t_2 ← V_{Se} energy gap is 1.18 eV (1050 nm), the Cu t_2 ← V_{Se}* gap is 2.33 eV (530 nm), and the Cu t_2 ← CB gap is 2.69 eV (460 nm). A labeled figure with these values can be found in the Supplemental Figure S6(a). These results confirm that the green PL observed in the emission spectrum is mainly due to the recombination of a hole trapped in the Cu t_2 state and the electron from the V_{Se}*. The V_{Se} bonding state apparently acts as an electron trap, causing a reduction on potential QY from these systems. It is likely that the Cu ← V_{Se}* and Cu ← VB both contribute to the green PL peak in these systems, however further discussion is continued supporting the former case below.

The DOS for the ZnSe:Cu,Al system was studied in a 64-atom supercell by replacing two Zn atoms with a Cu and an Al. Both atoms were distorted in the same direction toward three Se neighbors so the bond distances would be 2.35 Å. The fourth Se was distorted toward the Cu and Al with a bond distance of 2.67 Å. The calculated DOS are reported in Figure 5(b) along with the ZnSe DOS, for comparison. As before, the Se 2p and Cu d(e) states are hybridized and make up the VB edge. The Cu d(t_2) states are found at E_{VB} +0.45 eV, similar to the ZnSe:Cu system, as determined by Gaussian fitting. The Gaussian fit peaks and energy level labels can be seen in the Supplemental Figure S6(b). States associated with Al were found separate and below the CB edge at E_{VB} +2.38 eV. These states were made up of Al sp^3-hybridized orbitals. The integrated LDOS are shown in Figure 6. Again using the calculated E_g (2.48 eV) and experimental E_g as a correction factor, the Cu d(t_2) ← VB transition is expected at 480 nm, while the Cu d(t_2) ← Al is calculated to be 520 nm. These results confirm the DAP recombination mechanism in this system. It is also expected that the ZnSe:Cu,Al will have a slightly blue-shifted PL compared to the ZnSe:Cu due to the shallow donor state caused by Al being higher in energy than the V_{Se}* state. This result suggests that the emission in the ZnSe:Cu system is due, primarily, to the Cu ← V_{Se}* transition, as the ZnSe:Cu,Al PL is blue-shifted with respect to the ZnSe:Cu PL.

Time-Resolved Photoluminescence. The time-resolved PL of ZnSe:Cu and ZnSe:Cu,Al NCs was investigated using TCSPC. The fluorescence decay was monitored following photoexcitation at 395 nm, which is low enough to minimize initial hot electron relaxation. The PL decay traces were collected over the entire

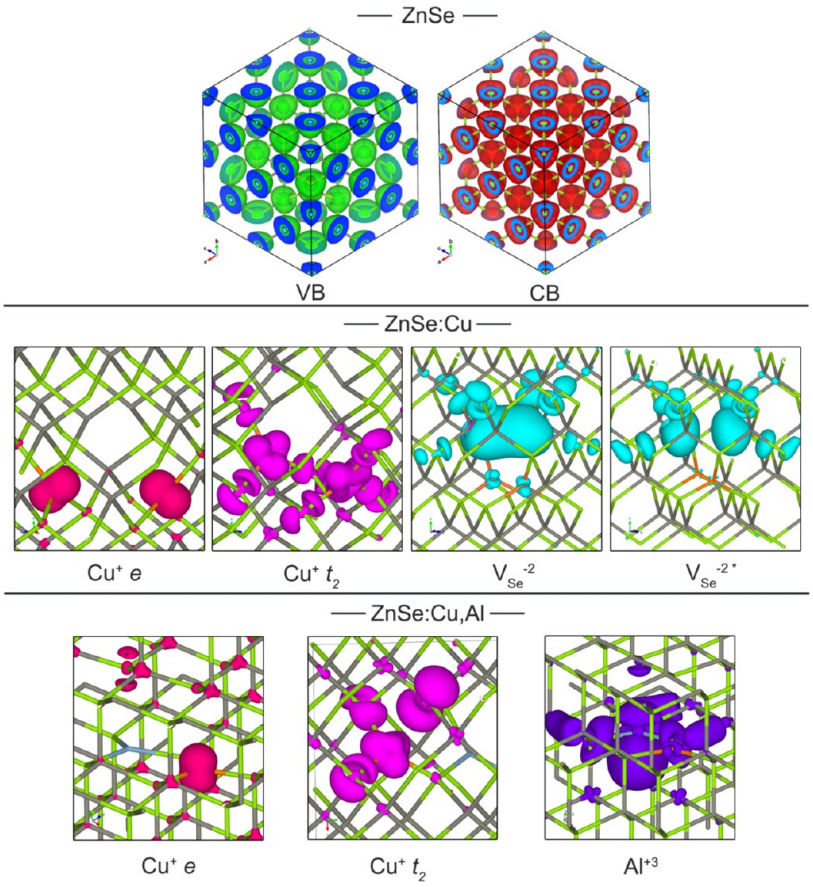

Figure 6. Integrated local density of states (LDOS) for the ZnSe VB and CB; ZnSe:Cu Cu^+ e and t_2 states and the $V_{Se^{2-}}$ state; and ZnSe:Cu,Al Cu^+ e and t_2 and Al^{3+} sp^3 hybrid orbitals. Atom colors are Zn (gray), Se (green), Cu (orange), and Al (blue).

wavelength range of the PL emission peak at a number of individual wavelengths. The time dependence of the normalized emission collected at 530 nm is shown in Figure 7(a) for both samples. The PL decay for both samples extends out to 1800 ns, which is orders of magnitude longer than the fluorescence lifetime observed in the host ZnSe.[31] It is evident that the inclusion of Al has a significant effect on the decay by increasing the lifetime of the recombination. To elucidate the effects of Al on the fluorescence process, the single-wavelength traces were fit with a triple-exponential function, eq 1, where $I(t)$ is the intensity as a function of time t, A_i is the initial PL intensity of the individual component, and τ_i is the lifetime of that component. The rise component was fit with the instrument response function as collected from a scattering sample consisting of a nondairy creamer. The results of the fit are shown in Figure 7(a).

$$I(t, \lambda) = \sum_{i=1}^{3} A_i(\lambda) e^{-t/\tau_i} \quad (1)$$

The two relatively fast decaying components are similar in both samples, which are 15 ± 1 and 100 ± 10 ns, and are attributed to recombination from ST and deep trap (DT) states, respectively. ST states might originate from Se vacancies, whereas Se dangling bonds on the NC surface give rise to DT states.[51] The lifetime for the slow decaying component, which is attributed to dopant-related emission, was found to increase from 550 ± 60 ns to 700 ± 60 ns after Al co-doping. Upon photoexcitation, Al acts as an electron trap, whereas Cu acts as a hole trap, giving rise to DAP emission. It is suggested that the efficiency of Al as an electron trap and the spatial proximity of the donor and acceptor levels could be the reason for increased PL QY and lengthened lifetime. However, the elimination of surface Cu and Se vacancies after co-doping could also affect the nonradiative recombination.

The wavelength dependence of the three time constants was examined by taking the lifetimes to be independent of the wavelength and examining the wavelength dependence of the initial amplitude alone. This procedure was carried out with an in-house-written procedure that utilizes singular value decomposition to obtain the orthogonal wavelength and time-dependent basis vectors, the latter of which are subsequently fit using a triple exponential function to obtain the wavelength-independent time constants reported. The SVD global fitting procedure provides the wavelength-dependent initial amplitude, referred

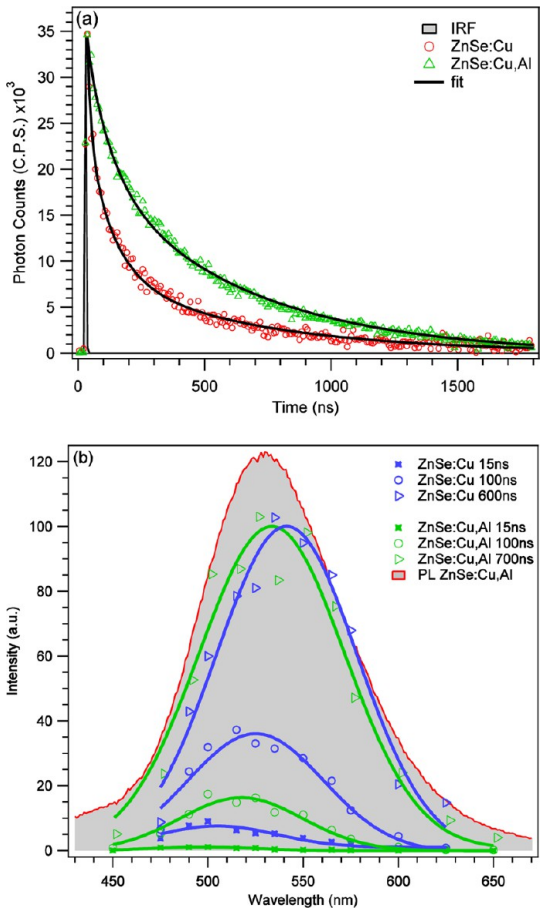

Figure 7. (a) PL decay traces of ZnSe:Cu and ZnSe:Cu,Al samples collected at 530 nm using a TCSPC system. Each trace required a triple-exponential function to achieve a good fit, which is plotted on top of each decay trace. (b) Spectral deconvolution representing the contribution of various lifetime components to the steady-state PL. The integrated PL from each component at each collected wavelength is plotted and fit with a Gaussian function.

to as the B-spectra. To examine the number of photons emitted by a given recombination process, which is directly related to the number of electron hole recombination events produced through a given process, the B-spectra (BS) were integrated with respect to the individual time constants to obtain the photon flux Φ_P, eq 2. The results of this analysis are shown in Figure 7(b).

$$\Phi_P(\lambda) = \mathrm{BS}(\lambda)\int e^{-t/\tau_i}\,dt \qquad (2)$$

The Φ_P data corresponding to each spectral component were then fit with a Gaussian function. It is quite obvious from the plot that the majority of the emitted photons correspond to the Cu impurity for both samples. Although there is some contribution from ST and DT state emissions (15 and 100 ns components), the ratios of trap state emissions to that of dopant emission vary considerably among the two samples.

The enhanced QY and decrease in the trap state emission could be explained on the basis of structural and electronic properties as revealed by EXAFS and DFT. In the ZnSe:Cu sample, Cu centers are associated with Se vacancies and ~1/4 of the Cu is on or near the surface of the NC, which can lead to nonradiative recombination. Al^{3+} co-doping not only compensates for the charge imbalance originating from Cu^+ doping, thus eliminating the Se vacancies associated with the Cu center, but also results in enhanced internal doping of Cu. This would lead to a decrease in the density of trap states and trap states related emission, as observed in the time-resolved PL data. In addition, Al acts as an efficient electron trap center, increasing DAP emission, thereby decreasing the probability of trap-mediated nonradiative recombination, and leads to enhanced QY.

CONCLUSIONS

A wet chemical method was used to synthesize ZnSe:Cu and ZnSe:Cu,Al quantum-confined NCs. XRD revealed a zinc blende structure and a particle size around 6 nm, which is further confirmed by TEM. XANES confirms that Cu is in a +1 oxidation state, and Al, in a +3 oxidation state, gets incorporated in the vicinity of the Cu site. For ZnSe:Cu NCs, EXAFS supports the existence of two types of Cu sites. One was the interior site where Cu ions occupy an off-centered tedrahedral site accompanying a Se vacancy. This accounts for approximately 3/4 of Cu content, whereas the remaining Cu^+ occupies a surface site. Co-doping with Al^{3+} results in internal doping; however, Cu^+ is neither substitutional nor interstitial but occupies a distorted Cu^+_{Zn} site close to three of the Se and displaced away from the fourth one. For both samples, the distortion leads to splitting of the second-neighbor peak to such an extent that real parts of the FT are no longer in phase, resulting in reduction of amplitude to almost negligible. Fitting the data by including an additional peak around 2.83 Å, corresponding to Cu_i^+ second neighbors, reveals that there is no considerable fraction of Cu_i^+.

Co-doping with Al was found to increase the QY by a factor of 2. Following photoexcitation, electrons become trapped at Al donor states, whereas Cu ions act as hole traps, leading to a DAP recombination. DFT calculations suggest that e d orbitals of Cu are strongly hybridized with the VB of the ZnSe NC and t_2 d orbitals act as the hole traps after photoexcitation. The efficiency of Al as an electron trap and spatial proximity of the donor and acceptor sites could be the origin of improved QY in ZnSe:Cu,Al. In addition, as revealed by EXAFS, without Al 1/3 of the Cu dopant atoms are on or near the surface, which tends to result in trap states that lead to decreased PL. TCSPC studies show that the PL decays follow a triple exponential for both samples. The lifetime constants related to the ZnSe trap states are similar for the two samples, but the lifetime

associated with dopant-related PL increases from 550 ns in ZnSe:Cu to 700 ns in ZnSe:Cu,Al. The enhancement of PL from co-doping not only is intriguing fundamentally but also opens up new avenues for the potential technological applications of doped semiconductor nanomaterials.

EXPERIMENTAL SECTION

Materials. Zinc stearate (technical grade), octadecene (ODE, 90%), tributylphosphine (TBP 97%, mixture of isomers), copper acetate (98%), octadecylamine (ODA, 99%), copper acetate (99.9%), and chloroform (anhydrous) were from Sigma-Aldrich. Se powder (<325 mesh, 99.7%) was purchased from Acros Organics, and anhydrous zinc acetate (99.98%), cuprous selenide (99.999%), cupric selenide (99.999%), aluminum tristearate (technical grade), aluminum oxide (99.97% metal basis), and boron nitride (99.5%) were bought from Alfa Aesar. Methanol (99.9%) and Acetone (99.7%) were purchased from Fisher Scientific. All the chemicals were used without further purification.

Synthesis of NCs. Doped ZnSe NCs were synthesized following the method of Peng *et al.*,[22] with some modification as reported previously.[31] Briefly, 0.12 g of zinc stearate in 20 mL of ODE was heated to 300 °C in a 50 mL three-neck flask under argon flow. To this solution of $ZnSt_2$ was injected a 3 mL degassed mixture of Se powder (0.080 g) dissolved in 0.80 g of TBP along with 0.30 g of ODA and diluted with ODE (2 mL). The heat was removed 30 s after the injection, and the mixture was cooled to 200 °C, at which point the sample was equally divided between two flasks, one part for making the Cu-doped sample and the second one for the Al co-doped sample. The purpose of using the ZnSe cores from the same batch for both doped and co-doped NCs was to minimize the subtle differences between the samples. For ZnSe:Cu, a calculated amount of a copper (Cu being 0.5% of total Zn content) stock solution (1.074×10^{-3} g of copper acetate dissolved in 1.25 g of TBP) was added dropwise to ZnSe cores at 200 °C. The temperature was then slowly ramped up to 240 °C and maintained for 2 h, during which 0.15 mL aliquots of zinc acetate solution (0.1 M solution in TBP diluted to 0.05 M with ODE) as well as selenium solution (as mentioned earlier) were added at regular intervals until no change was observed in the PL spectra. The Al co-doped sample was prepared the same way as ZnSe:Cu except that a calculated amount of aluminum stearate suspension (in ODE) was added along with a copper acetate solution. Also, a pure ZnSe sample was synthesized similarly without adding any impurities. To monitor the absorption and PL spectra, small aliquots (~0.2 mL) were taken from the flask with a syringe and diluted to an optical density between 0.2 and 0.3 at 390 nm using chloroform. The unreacted precursors were solvent extracted twice from the crude sample by mixing it with a mixture of chloroform and methanol (1:4). To isolate the solid particles, NCs in the ODE phase were precipitated using acetone, recovered by centrifuging, and stored under argon.

Structural and Spectroscopic Measurements. A Hewlett-Packard 8452A diode array spectrometer was used to measure the UV−visible spectra at room temperature. PL spectra were recorded using a Perkin-Elmer Luminescence spectrometer. PL QY of NCs was calculated by comparing the integrated PL intensity of the NCs (PL_{NC}) in chloroform to that of perylene dye in ethanol.[52] The absorption of the dye (Abs_{dye}) and each NC sample (Abs_{NC}) at the excitation wavelength (390 nm), the temperature, and the refractive indices of the solvents were taken into account for QY calculation using eq 3.

$$QY = QY_{dye} \frac{PL_{NC}}{PL_{dye}} \frac{Abs_{dye}}{Abs_{NC}} \frac{n_{chloroform}}{n_{ethanol}} \quad (3)$$

Low-resolution TEM measurements were performed on a JEOL model JEM-1200EX microscope at 80 kV. High-resolution TEM (HRTEM) images were obtained at Lawrence Berkeley National Laboratory using a Philips CM300-FEG at the National Center for Electron Microscopy.

Elemental analysis was performed with inductively coupled plasma optical emission spectroscopy (ICP-OES) using a Perkin-Elmer Optima 4300DV. To remove the excess precursors, NCs were repeatedly purified using a Sorvall RC-5C Plus centrifuge that was used at 14 000 rpm at room temperature to crash the NCs and then dried before digesting them in an Optima-grade HNO_3/HCl mixture (aqua regia). The digested samples were diluted with Milli-Q water and pumped at a rate of 1.5 mL/min into the plasma chamber.

A Rigaku Americas Miniflex Plus powder diffractometer was used for XRD measurements utilizing Cu Kα ($\lambda = 1.5405$ Å) as the incident radiation. Diffraction patterns were recorded at a rate of 2° per minute with a step size of 0.04°.

Zn and Cu K-edge XANES and EXAFS data were collected at the Stanford Synchrotron Radiation Lightsource (SSRL), on beamline 7-3 at 10 K with an average current of 300 mA and at an electron energy of 3.0 GeV. The radiation was monochromatized using a Si (220) double crystal monochromator, which was detuned to 50% of its maximum at the Zn/Cu K-edge to minimize the effects of higher harmonics. The beam size on the sample was reduced to 0.5 mm vertical and 1.0 mm horizontal fwhm, and the intensity of the incident X-rays (I_0) was monitored by a N_2-filled ion chamber in front of the sample. Zn data were collected in transmission mode, whereas, due to low concentration, Cu data were collected in fluorescence mode using a 30-element Ge detector (Canberra), with the samples at 45° to the incident beam. The energy was calibrated by using the rising edge positions of Cu foil (8980.3 eV) and Zn foil (9660.7 eV). Cu K-edge data were collected for NC samples along with those of Cu_2Se and CuSe standards. For the EXAFS studies, samples were deposited in plexiglass sample holders with Kapton film windows. In the case of Cu_2Se and CuSe standards, the samples were diluted with boron nitride to a concentration of 0.3% and sandwiched between two layers of Mylar tape.

Standard programs[53] based on the IFEFFIT library,[54] were used for data reduction and fitting. While reducing fluorescence data, the pre-edge background was fit to a line with a constant baseline, whereas the post-edge background was fitted to a spline function. In the case of transmission data, the pre-edge and post-edge backgrounds were fit to a Victoreen and spline function, respectively. The extracted k-space data, $k^3\chi(k)$, averaged over 5 scans, was then used to FT the data into r-space. For the Zn K-edge, a k-space window of 3.5−14.0 $Å^{-1}$ was used for FT, whereas for Cu K-edge data the FT range used was 3.5−11.0 $Å^{-1}$. The window function used consisted of a rectangular part in the center and Hanning parts on the sides having a Hanning fraction[55] of 0.2.

X-ray absorption spectra at the Al K-edge were measured on beamline 6.3.1 at the Advanced Light Source at Lawrence Berkeley National Laboratory. The data were collected in partial fluorescence yield (PFY) mode using a silicon drift detector (SII Vortex), and total electron yield (TEY) mode by monitoring the sample drain current. The beamline resolution was set to ~1.0 eV at the Al K-edge. Photocurrent from a gold mesh, inserted in the beamline before the sample, was used to normalize the spectra. The XAS spectrum of 0.4 μm Al metal foil was used for energy calibration.

Time-resolved PL studies of the ZnSe:Cu and ZnSe:Cu,Al samples were performed at room temperature using TCSPC as described in our previous report.[31] Briefly, a Ti:sapphire crystal (Kapteyn-Murnane Laboratories, model MTS Mini Ti:Saphire) was pumped with a 5 W Coherent Verdi-V5 (532 nm) laser to produce a tunable, mode-locked laser line between 790 and 820 nm with a frequency of 100 MHz. A pulse picker (Conoptics, model 350-160) was utilized to prepare a pulse train of 0.5 MHz, after which the 790 nm light was frequency doubled to 395 nm using a BiBO crystal. After separating the 790 and 395 nm light with a dichroic mirror, the 395 nm (50 ps pulse width) was then

used to excite the NC sample in chloroform. The PL was collected at 90° with respect to the incident laser and passed through a magic angle polarizer followed by a monochromator with a resolution of 0.25 nm. The monochromatic light was then focused on an avalanche photodiode, where photons were counted in a reverse stop−start mode.[56]

A number of time windows were collected to investigate the wide range of time constants observed in the decay spectrum of these samples and were 50, 380, and 2000 ns for individual emission wavelengths ranging from 450 to 650 nm. The NCs were probed using a 50 ns window over 4096 channels, 380 and 1000 ns windows over 1024 channels, and a 2000 ns window over 256 channels. The instrumental resolutions were 0.05, 0.32, and 0.70 ns for 50, 380, and 2000 ns time windows, respectively. Data were analyzed using an IGOR Pro-based (wavemetrics) macroprocedure developed in-house.

Conflict of Interest: The authors declare no competing financial interest.

Acknowledgment. This project was funded by the U.S. Department of Energy under contract no. DE-FG02-07ER46388-A002. For the use of the HRTEM facilities, we are grateful to Chenyou Song and the authorities at National Center for Electron Microscopy and Advanced Light Source, Lawrence Berkeley National Laboratory, which is supported by the U.S. Department of Energy under contract number DE-AC02-05CH11231. The EXAFS measurements were carried out at the Stanford Synchrotron Radiation Light Source, a Directorate of SLAC National Accelerator Laboratory and an Office of Science User Facility operated for the U.S. Department of Energy Office of Science by Stanford University. DFT calculations were performed on the UCSC campusrocks cluster. A special thank you to Burak Himmetoglu is deserved and a debt of gratitude owed for his kind assistance with Quantum Espresso and generous offerings of his depth of DFT knowledge.

Supporting Information Available: Fit parameters for Zn and Cu EXAFS (Table S1). Cu EXAFS data of ZnSe:Cu along with fit #1 without including Cu−O path (Figure S1) and fit #3 covering the long-range (Figure S2). Cu EXAFS data for ZnSe:Cu,Al including the fit, assuming substitutional Cu (Figure S3) and distorted Cu (Figure S4). DOS for Cu d orbitals in ZnSe:Cu 64-atom unit cell (Figure S5). DOS for ZnSe:Cu and ZnSe:Cu,Al showing the energy difference between different levels (Figure S6). This material is available free of charge *via* the Internet at http://pubs.acs.org.

REFERENCES AND NOTES

1. Klimov, V. I.; Ivanov, S. A.; Nanda, J.; Achermann, M.; Bezel, I.; McGuire, J. A.; Piryatinski, A. Single-Exciton Optical Gain in Semiconductor Nanocrystals. *Nature* **2007**, *447*, 441–446.
2. Burda, C.; Chen, X.; Narayanan, R.; El-Sayed, M. A. Chemistry and Properties of Nanocrystals of Different Shapes. *Chem. Rev. (Washington, DC, U. S.)* **2005**, *105*, 1025–1102.
3. Chen, C. C.; Herhold, A. B.; Johnson, C. S.; Alivisatos, A. P. Size Dependence of Structural Metastability in Semiconductor Nanocrystals. *Science* **1997**, *276*, 398–401.
4. Nirmal, M.; Dabbousi, B. O.; Bawendi, M. G.; Macklin, J. J.; Trautman, J. K.; Harris, T. D.; Brus, L. E. Fluorescence Intermittency in Single Cadmium Selenide Nanocrystals. *Nature* **1996**, *383*, 802–804.
5. Alivisatos, A. P. Semiconductor Clusters, Nanocrystals, and Quantum Dots. *Science* **1996**, *271*, 933–937.
6. Shim, M.; Wang, C.; Guyot-Sionnest, P. Charge-Tunable Optical Properties in Colloidal Semiconductor Nanocrystals. *J. Phys. Chem. B* **2001**, *105*, 2369–2373.
7. Murray, C. B.; Norris, D. J.; Bawendi, M. G. Synthesis and Characterization of Nearly Monodisperse CdE (E = Sulfur, Selenium, Tellurium) Semiconductor Nanocrystallites. *J. Am. Chem. Soc.* **1993**, *115*, 8706–8715.
8. Kim, T. H.; Cho, K. S.; Lee, E. K.; Lee, S. J.; Chae, J.; Kim, J. W.; Kwon, J. Y.; Amaratunga, G.; Lee, S. Y.; Choi, B. L. Full-Colour Quantum Dot Displays Fabricated by Transfer Printing. *Nat. Photonics* **2011**, *5*, 176–182.
9. Brovelli, S.; Chiodini, N.; Lorenzi, R.; Lauria, A.; Romagnoli, M.; Paleari, A. Fully Inorganic Oxide-in-Oxide Ultraviolet Nanocrystal Light Emitting Devices. *Nat. Commun.* **2012**, *3*, 690.
10. Alivisatos, P. The Use of Nanocrystals in Biological Detection. *Nat. Biotechnol.* **2003**, *22*, 47–52.
11. Chan, W. C. W.; Nie, S. Quantum Dot Bioconjugates for Ultrasensitive Nonisotopic Detection. *Science* **1998**, *281*, 2016–2018.
12. Pradhan, N.; Battaglia, D. M.; Liu, Y.; Peng, X. Efficient, Stable, Small, and Water-Soluble Doped ZnSe Nanocrystal Emitters as Non-Cadmium Biomedical Labels. *Nano Lett.* **2007**, *7*, 312–317.
13. Gur, I.; Fromer, N. A.; Geier, M. L.; Alivisatos, A. P. Air-Stable All-Inorganic Nanocrystal Solar Cells Processed from Solution. *Science* **2005**, *310*, 462–465.
14. Luther, J. M.; Law, M.; Beard, M. C.; Song, Q.; Reese, M. O.; Ellingson, R. J.; Nozik, A. J. Schottky Solar Cells Based on Colloidal Nanocrystal Films. *Nano Lett.* **2008**, *8*, 3488–3492.
15. Talapin, D. V.; Lee, J.-S.; Kovalenko, M. V.; Shevchenko, E. V. Prospects of Colloidal Nanocrystals for Electronic and Optoelectronic Applications. *Chem. Rev. (Washington, DC, U. S.)* **2009**, *110*, 389–458.
16. Wang, Y.; Herron, N.; Moller, K.; Bein, T. Three-Dimensionally Confined Diluted Magnetic Semiconductor Clusters: $Zn_{1-x}Mn_xS$. *Solid State Commun.* **1991**, *77*, 33–38.
17. Erwin, S. C.; Zu, L.; Haftel, M. I.; Efros, A. L.; Kennedy, T. A.; Norris, D. J. Doping Semiconductor Nanocrystals. *Nature* **2005**, *436*, 91–94.
18. Smith, B. A.; Zhang, J. Z.; Joly, A.; Liu, J. Luminescence Decay Kinetics of Mn^{2+}-Doped ZnS Nanoclusters Grown in Reverse Micelles. *Phys. Rev. B* **2000**, *62*, 2021–2028.
19. Chen, W.; Zhang, J. Z.; Joly, A. G. Optical Properties and Potential Applications of Doped Semiconductor Nanoparticles. *J. Nanosci. Nanotechnol.* **2004**, *4*, 919–947.
20. Schwartz, D. A.; Norberg, N. S.; Nguyen, Q. P.; Parker, J. M.; Gamelin, D. R. Magnetic Quantum Dots: Synthesis, Spectroscopy, and Magnetism of Co^{2+}- and Ni^{2+}-Doped ZnO Nanocrystals. *J. Am. Chem. Soc.* **2003**, *125*, 13205–13218.
21. Bhargava, R. N.; Gallagher, D.; Hong, X.; Nurmikko, A. Optical Properties of Manganese-Doped Nanocrystals of ZnS. *Phys. Rev. Lett.* **1994**, *72*, 416–419.
22. Pradhan, N.; Goorskey, D.; Thessing, J.; Peng, X. An Alternative of CdSe Nanocrystal Emitters: Pure and Tunable Impurity Emissions in ZnSe Nanocrystals. *J. Am. Chem. Soc.* **2005**, *127*, 17586–17587.
23. Sooklal, K.; Cullum, B. S.; Angel, S. M.; Murphy, C. J. Photophysical Properties of ZnS Nanoclusters with Spatially Localized Mn^{2+}. *J. Phys. Chem.* **1996**, *100*, 4551–4555.
24. Norris, D.; Yao, N.; Charnock, F.; Kennedy, T. High-Quality Manganese-Doped ZnSe Nanocrystals. *Nano Lett.* **2001**, *1*, 3–7.
25. Viswanatha, R.; Brovelli, S.; Pandey, A.; Crooker, S. A.; Klimov, V. I. Copper-Doped Inverted Core/Shell Nanocrystals with "Permanent" Optically Active Holes. *Nano Lett.* **2011**, *11*, 4753–4758.
26. Brovelli, S.; Galland, C.; Viswanatha, R.; Klimov, V. I. Tuning Radiative Recombination in Cu-Doped Nanocrystals *via* Electrochemical Control of Surface Trapping. *Nano Lett.* **2012**, *12*, 4372–4379.
27. Bhaumik, S.; Ghosh, B.; Pal, A. J. Color Tunable Light-Emitting Diodes Based on Copper Doped Semiconducting Nanocrystals. *Appl. Phys. Lett.* **2011**, *99*, 083106–083106−3.
28. Panda, S. K.; Hickey, S. G.; Demir, H. V.; Eychmüller, A. Bright White-Light Emitting Manganese and Copper Co-Doped ZnSe Quantum Dots. *Angew. Chem.* **2011**, *123*, 4524–4528.
29. *System Analyzer*; OLI Systems Inc.: Morris Plains, NJ, 2009.
30. Lide, D. R. *CRC Handbook of Chemistry and Physics*; Taylor and Francis: Boca Raton, FL, 2006−2007.
31. Gul, S.; Cooper, J. K.; Corrado, C.; Vollbrecht, B.; Bridges, F.; Guo, J.; Zhang, J. Z. Synthesis, Optical and Structural Properties, and Charge Carrier Dynamics of Cu-Doped ZnSe Nanocrystals. *J. Phys. Chem. C* **2011**, *115*, 20864–20875.

32. Hoogenstraaten, W. The Chemistry of Traps in Zinc Sulfide Phosphors. *J. Electrochem. Soc.* **1953**, *100*, 356–365.
33. Godlewski, M.; Lamb, W.; Cavenett, B. ODMR Investigations of Recombination Processes in ZnSe:Cu. *Solid State Commun.* **1981**, *39*, 595–599.
34. Corrado, C.; Jiang, Y.; Oba, F.; Kozina, M.; Bridges, F.; Zhang, J. Z. Synthesis, Structural, and Optical Properties of Stable ZnS:Cu, Cl Nanocrystals. *J. Phys. Chem. A* **2009**, *113*, 3830–3839.
35. Corrado, C.; Hawker, M.; Livingston, G.; Medling, S.; Bridges, F.; Zhang, J. Z. Enhanced Cu Emission in ZnS:Cu,Cl/ZnS Core-Shell Nanocrystals. *Nanoscale* **2010**, *2*, 1213–1221.
36. Morozova, N.; Karetnikov, I.; Blinov, V.; Gavrishchuk, E. A Study of Luminescence Centers Related to Copper and Oxygen in ZnSe. *Semiconductors* **2001**, *35*, 24–32.
37. Jones, G.; Woods, J. The Luminescence of Self-Activated and Copper-Doped Zinc Selenide. *J. Lumin.* **1974**, *9*, 389–405.
38. Abràmoff, M. D.; Magalhães, P. J.; Ram, S. J. Image Processing with ImageJ. *Biophotonics Int.* **2004**, *11*, 36–42.
39. Kau, L. S.; Spira-Solomon, D. J.; Penner-Hahn, J. E.; Hodgson, K. O.; Solomon, E. I. X-Ray Absorption Edge Determination of the Oxidation State and Coordination Number of Copper. Application to the Type 3 Site in Rhus Vernicifera Laccase and Its Reaction with Oxygen. *J. Am. Chem. Soc.* **1987**, *109*, 6433–6442.
40. Bocharov, S.; Kirchner, T.; Dräger, G.; Šipr, O.; Šimunek, A. Dipole and Quadrupole Contributions to Polarized Cu K X-Ray Absorption near-Edge Structure Spectra of CuO. *Phys. Rev. B* **2001**, *63*, 045104.
41. Sarangi, R.; Aboelella, N.; Fujisawa, K.; Tolman, W. B.; Hedman, B.; Hodgson, K. O.; Solomon, E. I. X-Ray Absorption Edge Spectroscopy and Computational Studies on $LCuO_2$ Species: Superoxide-Cu(II) *versus* Peroxide-Cu(III) Bonding. *J. Am. Chem. Soc.* **2006**, *128*, 8286–8296.
42. Teo, B. K. *EXAFS: Basic Principles and Data Analysis*; Springer-Verlag: Berlin, 1986; pp 26−27.
43. Zabinsky, S. I.; Rehr, J. J.; Ankudinov, A.; Albers, R. C.; Eller, M. J. Multiple-Scattering Calculations of X-Ray-Absorption Spectra. *Phys. Rev. B* **1995**, *52*, 2995–3009.
44. Diop, D.; Grisenti, R. EXAFS Debye-Waller Factor of ZnSe. *Phys. B* **1995**, *208−209*, 164–166.
45. Goldman, A.; Canova, E.; Kao, Y.; Fitzpatrick, B.; Bhargava, R.; Phillips, J. C. Extended X-Ray Absorption Fine Structure Studies of Diffused Copper Impurities in ZnSe. *Appl. Phys. Lett.* **1983**, *43*, 836–838.
46. Shionoya, S.; Urabe, K.; Koda, T.; Era, K.; Fujiwara, H. Nature of the Red-Copper Luminescence Centre in ZnS Crystals as Elucidated by Polarization Measurements. *J. Phys. Chem. Solids* **1966**, *27*, 865–869.
47. Urabe, K.; Shionoya, S.; Suzuki, A. Polarization of the Blue-Copper Luminescence in ZnS Crystals. *J. Phys. Soc. Jpn.* **1968**, *25*, 1611–1617.
48. Patel, J.; Davies, J.; Nicholls, J. Direct Optically Detected Magnetic Resonance Observation of a Copper Centre Associated with the Green Emission in ZnSe. *J. Phys. C: Solid State Phys.* **1981**, *14*, 5545–5557.
49. Car, B.; Medling, S.; Corrado, C.; Bridges, F.; Zhang, J. Z. Probing the Local Structure of Dilute Cu Dopants in Fluorescent ZnS Nanocrystals Using EXAFS. *Nanoscale* **2011**, *3*, 4182–4189.
50. Gulay, L.; Daszkiewicz, M.; Strok, O.; Pietraszko, A. Crystal Structure of Cu_2Se. *Chem. Met. Alloys* **2011**, *4*, 200–205.
51. Underwood, D. F.; Kippeny, T.; Rosenthal, S. J. Ultrafast Carrier Dynamics in CdSe Nanocrystals Determined by Femtosecond Fluorescence Upconversion Spectroscopy. *J. Phys. Chem. B* **2001**, *105*, 436–443.
52. Magde, D.; Wong, R.; Seybold, P. G. Fluorescence Quantum Yields and Their Relation to Lifetimes of Rhodamine 6G and Fluorescein in Nine Solvents: Improved Absolute Standards for Quantum Yields. *Photochem. Photobiol.* **2002**, *75*, 327–334.
53. Ravel, B.; Newville, M. ATHENA, ARTEMIS, HEPHAESTUS: Data Analysis for X-Ray Absorption Spectroscopy Using IFEFFIT. *J. Synchrotron Radiat.* **2005**, *12*, 537–541.
54. Newville, M. IFEFFIT: Interactive XAFS Analysis and FEFF Fitting. *J. Synchrotron Radiat.* **2001**, *8*, 322–324.
55. Koningsberger, D.; Prins, R. *X-Ray Absorption: Principles, Applications, Techniques of EXAFS, SEXAFS and XANES*; John Wiley and Sons: New York, 1988; pp 231−232.
56. Becker, W. *Advanced Time-Correlated Single Photon Counting Techniques*; Springer: Berlin, 2005.